Mon. Not. R. Astron. Soc. **347,** 824–832 (2004)

The relationship between the Sérsic law profiles measured along the major and minor axes of elliptical galaxies

F. Ferrari,[1]★† H. Dottori,[1] N. Caon,[2] A. Nobrega[1,3] and D. B. Pavani[1]‡

[1]*Instituto de Física – UFRGS, Av. Bento Gonçalves, 9500 Porto Alegre RS, Brazil*
[2]*Instituto de Astrofísica de Canarias, Via Lactéa, E-38200 La Laguna, Tenerife, Canary Islands, Spain*
[3]*CETEC – UNOCHAPECÓ, Av. Senador Attílio Fontana, s/n, Chapecó SC, Brazil*

Accepted 2003 September 30. Received 2003 September 30; in original form 2002 May 17

ABSTRACT

In this paper we discuss the reason why the parameters of the Sérsic model best-fitting the major axis light profile of elliptical galaxies can differ significantly from those derived for the minor axis profile. We show that this discrepancy is a natural consequence of the fact that the isophote eccentricity varies with the radius of the isophote and present a mathematical transformation that allows the minor axis Sérsic model to be calculated from the major axis model, provided that the elliptical isophotes are aligned and concentric and that their eccentricity can be represented by a well behaved, though quite general, function of the radius. When there is no variation in eccentricity only the effective radius changes in the Sérsic model, while for radial-dependent eccentricity the transformation, which allows the minor axis Sérsic model to be calculated from the major axis model is given by the Lerch Φ transcendental function. The proposed transformation was tested using photometric data for 28 early-type galaxies.

Key words: galaxies: fundamental parameters – galaxies: photometry – galaxies: structure.

1 INTRODUCTION

It is now recognized that the de Vaucouleurs (1948) $R^{1/4}$ law does not fit the observed light distribution of elliptical galaxies (e.g. Schombert 1986). A much better representation of the light distribution in bright and dwarf elliptical galaxies and the bulges of spiral galaxies is provided by the Sérsic (1968) law:

$$\log\left(\frac{I(R)}{I_n}\right) = -b_n\left[\left(\frac{R}{R_n}\right)^{1/n} - 1\right], \quad (1)$$

where R_n is the radius encircling half the total galaxy luminosity and I_n is the intensity at R_n. The coefficient b_n is a function of n, which can be approximated by the relation $b_n \simeq 2n - 0.327$ (Ciotti 1991).

The shape index n, which parametrizes the curvature of the Sérsic model has been shown to correlate with the luminosity and size of the galaxy – brighter and larger galaxies having larger values of n (Caon, Capaccioli & D'Onofrio 1993, subsequently cited as CCD93) – and also, notably, with the central velocity dispersion σ_0 and the mass of the central supermassive black hole (Graham, Trujillo & Caon 2001a; Graham et al. 2001b).

An important source of uncertainty affecting the determination of parameters of the Sérsic model that best describes the light distribution of a galaxy, is on which axis (major, minor or equivalent) the light profile should be fitted.

CCD93 extensively studied the light profiles of many Virgo cluster E and S0 galaxies by independently fitting Sérsic models to their major and minor axes, finding that in ∼40 per cent of the galaxies there were large discrepancies between the Sérsic parameters determined along the major and the minor axes. Such discrepancies were found not only among S0 galaxies, which could be misclassified as E galaxies but also among genuine elliptical galaxies such as the E4 galaxy NGC 4621 and E3 galaxy NGC 4406.

Eccentricity gradients imply that both the major and minor axes cannot be, for example, described by the $R^{1/4}$ model. The long observed ellipticity gradients in elliptical galaxies implies that the $R^{1/4}$ model cannot be universal, but this obvious fact has been largely ignored in the literature.

In this paper we demonstrate that the discrepancy between the major and the minor axes Sérsic models in elliptical galaxies can be accounted for by radial variations of the eccentricity of the isophotes. We also present a mathematical formula that, coupled with the eccentricity profile, permits the transformation of the major axis Sérsic model into the minor axis model, provided that the galaxy has well-behaved isophotes, where the eccentricity varies with radius, but which have the same centre and position angle.

In Section 2 we describe the proposed mathematical transformation, the applicability and validity of which is tested using a sample of galaxies selected from those studied by CCD93, as described in Section 3. In Section 4 we present the fitting method and in Section 5 we analyse and discuss our results.

★E-mail: ferrari@if.ufrgs.br
†Programa Institutos do Milênio – MCT/CNPq/PADCT.
‡CNPq fellow.

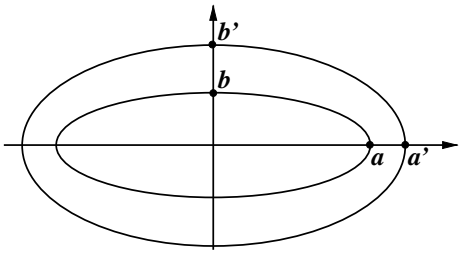

Figure 1. Two isophotes with major and minor axes (a, b) and (a', b').

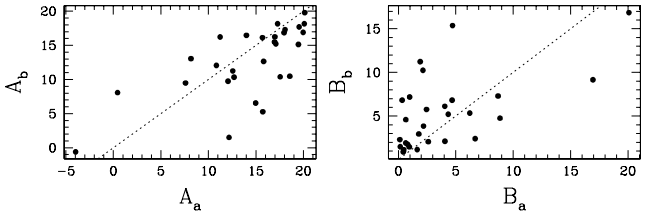

Figure 2. The relationship between the Sérsic parameters of equation (2). The subscript a refers to the major axis and subscript b to the minor axis.

2 THE LINK BETWEEN MAJOR AND MINOR AXES SÉRSIC PROFILES

A simpler and more convenient representation of the Sérsic law is the form given in CCD93:

$$\mu(R) = A + BR^{1/n}, \tag{2}$$

where, according to equation (1), $A = -2.5(b_n + \log I_n)$, $B = 2.5b_n/R_n^{1/n}$. R may represent the radial variable along the semi-major axis a, the semi-minor axis b or the equivalent radius $\sqrt{ab}$. The differential of the surface brightness profile can then be written as

$$\mathrm{d}\mu(R) = \frac{B}{n} R^{1/n-1}\,\mathrm{d}R. \tag{3}$$

Consider two nearby isophotes where the major and minor axes are, respectively, a and b for the inner isophote, and a' and b' for the outer one, as sketched in Fig. 1. The surface brightness gradient along the major axis may be written as

$$\frac{\mathrm{d}\mu}{\mathrm{d}a} = \lim_{\Delta a \to 0} \frac{\mu(a') - \mu(a)}{\Delta a} \tag{4}$$

with a similar expression holding true for the minor axis (b).

From the definition of an isophote, we know that $\mu(a) = \mu(b)$ and $\mu(a') = \mu(b')$, so the numerators in the right-hand side of expression (4) and in the equivalent expression for b are equal, while the denominators Δa and Δb will differ according to the radial behaviour of the eccentricity[1] $e(a) \equiv b/a$. In general, we have:

$$\frac{\mathrm{d}\mu(b)}{\mathrm{d}b} = \frac{1}{\mathcal{F}(a)} \frac{\mathrm{d}\mu(a)}{\mathrm{d}a}, \tag{5}$$

where $\mathcal{F}(a)$ will depend on the eccentricity function $e(a)$. We discuss the case of constant and variable eccentricity functions in the following sections.

2.1 Constant eccentricity

The simplest case is that of concentric isophotes having constant eccentricity. If the eccentricity $e \equiv b/a = e_\mathrm{c}$ is constant, then we have $b = e_\mathrm{c} a$ and $\mathrm{d}b = e_\mathrm{c}\,\mathrm{d}a$, thus:

$$\frac{\mathrm{d}\mu(b)}{\mathrm{d}b} = \frac{1}{e_\mathrm{c}} \frac{\mathrm{d}\mu(a)}{\mathrm{d}a}. \tag{6}$$

By direct integration of equations (2) and (6), we see that in this case the Sérsic index n will be the same along the major (a) and the minor (b) axes, $n_a = n_b$, and that the B coefficients on the major and minor axes are related by: $B_b = B_a/e_\mathrm{c}$. Equation (6) shows that the values of B obtained from the fits along the major and minor axes should not be considered to be independent of each other, as was implicitly assumed by CCD93 (see Section 4). By analysing the relationship between B and b_n in equations (1) and (2), it can be seen that the effect of e_c is to stretch out the relationship between B_a and B_b (Fig. 2).

Theoretically, the integration constants should be equal, i.e. $A_a = A_b$, since $\mu(a=0) = \mu(b=0)$. However, in real cases (e.g. CCD93) this equality is broken by a variety of observational uncertainties and practical constraints (for instance, light profiles are fitted within a surface brightness interval the limits of which differ, in general, on the major and minor axes). Consequently, different values for A_a and A_b are obtained when the fitted profile is extrapolated to $R = 0$.

The Sérsic model along the minor axis is related to the Sérsic model along the major axis by the equation:

$$\mu(b) = A_a + \frac{B_a}{e_\mathrm{c}} b^{1/n_a}, \tag{7}$$

where n_a is the major axis Sérsic index.

2.2 Variable eccentricity

In most galaxies, eccentricity is neither constant, nor is it a simple function of the radius. Indeed, no general rules seem to govern the radial variation of e, and it is not clear what the physical significance of this variation is Binney & Merrifield (1998). In cD galaxies, e generally decreases from the centre outwards, while in other galaxies $e(R)$ may increase, and sometimes it is found to vary non-monotonically with the radius.

Now, if the eccentricity is a differentiable function $e = e(a)$, then $\mathrm{d}b = e(a)\mathrm{d}a + a\mathrm{d}e$ or, equivalently,

$$\mathrm{d}b = \left[e(a) + a\frac{\mathrm{d}e}{\mathrm{d}a}\right] \mathrm{d}a \equiv \mathcal{F}(a)\,\mathrm{d}a. \tag{8}$$

In this case, the minor axis profile may have a very different shape from that of the major axis, depending on the form of function $e(a)$. We have integrated equation (5) for a general case in which $e(a)$ can be expressed as a function of the form

$$e(a) = e_0 + (e_1 - e_0)\left(\frac{a}{a_\mathrm{M}}\right)^l, \tag{9}$$

where a_M is the scalelength where the eccentricity equals e_1. Depending on l, e_0 and e_1, equation (9) may describe radial increasing ($e_0 < e_1$) or decreasing ($e_0 > e_1$) eccentricities, with different slopes. From equations (8) and (9) we can derive:

$$\frac{\mathrm{d}b}{\mathrm{d}a} = e_0 + (1+l)(e_1 - e_0)\left(\frac{a}{a_\mathrm{M}}\right)^l, \tag{10}$$

from which it follows

$$\frac{\mathrm{d}\mu}{\mathrm{d}b} = \left[e_0 + (1+l)(e_1 - e_0)\left(\frac{a}{a_\mathrm{M}}\right)^l\right]^{-1} \frac{\mathrm{d}\mu}{\mathrm{d}a}. \tag{11}$$

[1] For analytical simplicity, we use the eccentricity $e \equiv b/a$ instead of ellipticity $\varepsilon \equiv 1 - e$.

By comparing equations (5) and (11) we obtain $\mathcal{F}(a)$,

$$\mathcal{F}(a) = e_0 + (1+l)(e_1 - e_0)\left(\frac{a}{a_{\rm M}}\right)^l \tag{12}$$

We can integrate equation (11) in terms of the transcendental function Lerch Φ (Gradshteyn & Ryzhik 2000, see Appendix A), obtaining:

$$\mu_L(b) = A_a + \frac{B_a}{e_0 n_a l} a^{1/n_a}\,\Phi\left(1 - \frac{\mathcal{F}(a)}{e_0}; 1; \frac{1}{n_a l}\right) \tag{13}$$

The variable b does not appear explicitly on the right-hand side of this equation; in order to compute μ at a given distance b' on the minor axis, we should set the variable a on the right-hand side to that value of a' for which $b' = e(a')a'$.

Equation (13) shows how the major axis Sérsic law is modulated by the Lerch Φ function to give the minor axis light profile. By comparing it with the Sérsic law for the minor axis: $\mu(b) = A_b + B_b b^{1/n_b}$ (equation 2), we can write:

$$\begin{aligned} A_b &\iff A_a \\ B_b &\iff \frac{B_a}{e_0 n_a l} \\ b^{1/n_b} &\iff a^{1/n_a}\,\Phi\left(1 - \frac{\mathcal{F}(a)}{e_0}; 1; \frac{1}{n_a l}\right). \end{aligned} \tag{14}$$

2.3 The equivalent-axis Sérsic profile

The Sérsic law can also be expressed as a function of the equivalent radius, defined as $R_{\rm eq} = \sqrt{ab}$. In the case of constant eccentricity, $e(a) = e_{\rm c} =$ constant, equation (6) can be written as

$$\frac{{\rm d}\mu}{{\rm d}R_{\rm eq}} = \frac{1}{\sqrt{e_{\rm c}}}\frac{{\rm d}\mu(a)}{{\rm d}a}, \tag{15}$$

while, for variable eccentricity, equation (11) can be expressed as

$$\frac{{\rm d}\mu}{{\rm d}R_{\rm eq}} = \frac{2\sqrt{e(a)}}{e(a) + \mathcal{F}(a)}\,\frac{{\rm d}\mu}{{\rm d}a}, \tag{16}$$

where $e(a)$ is given by equation (9) and $\mathcal{F}(a)$ by equation (12). We were not able to integrate equation (16).

3 DATA SET USED

We applied the algorithm developed in the previous section to 28 galaxies selected from those studied by CCD93. Surface brightness and ellipticity profiles for these objects were published by Caon, Capaccioli & Rampazzo (1990) and Caon, Capaccioli & D'Onofrio (1994). The sample we use covered a wide interval of absolute magnitudes ($-22.43 < M_B < -17.29$) and included at least one object for each morphological type (E0 to E7, dS0 and S0).

The correspondence between the Sérsic model index n for the major (a) and minor (b) axis also varied: $n_a > n_b$ for eight galaxies; $n_a < n_b$ for 17, and $n_a \simeq n_b$ for three. The eccentricity (Fig. A1) increased with radius for 12 objects, decreased for another 12 and remained approximately constant for 4. The central parts of the light profiles, affected by seeing convolution, were excluded when fitting our eccentricity model (equation 9) to the observed profiles.

3.1 Errors

The photometric uncertainties on the CCD93 B-band surface brightness measurements were estimated by Caon et al. (1990), and are shown in fig. 3 of their paper. They can be approximated by the power-law function:

$$\delta\mu = \alpha\mu^\beta, \tag{17}$$

where $\delta\mu$ is the error, μ the surface brightness in magnitudes, $\alpha \simeq 3.25 \times 10^{-15}$ and $\beta \simeq 9.7$.

The error in the eccentricity can be estimated by approximating the differentials in equation (3) by small variations, i.e. ${\rm d}\mu \approx \delta\mu$ and ${\rm d}R \approx \delta R$, thus obtaining $\delta\mu = (B/n)R^{1/n-1}\delta R$. Rearranging the terms with the help of equation (17) we can write the fractional error $\delta R/R$ as

$$\frac{\delta R}{R} = \frac{n\alpha\mu^\beta}{BR^{1/n}} = \frac{n\alpha(A + BR^{1/n})^\beta}{BR^{1/n}}, \tag{18}$$

where R may be the a or b variable and the coefficients A, B, n may refer to the major or minor axis accordingly. Since the eccentricity is calculated as the quotient b/a, the fractional uncertainties add to give:

$$\frac{\delta e}{e} \approx \frac{\delta a}{a} + \frac{\delta b}{b}. \tag{19}$$

For example, in the outer parts ($a = 296$, $b = 180$ arcsec) of NGC 4473 we have $\delta\mu(a) \simeq 0.31$, $\delta\mu(b) \simeq 0.43$magarcsec^{-2}, $\delta a/a \simeq 0.08$ and $\delta b/b \simeq 0.15$, which yields $\delta e/e \simeq 0.23$. For NGC 4406 ($a = 510$, $b = 330$arcsec), $\delta\mu(a) = 0.17$, $\delta\mu(b) = 0.28$ mag arcsec^{-2}, $\delta a/a \simeq 0.06$ and $\delta b/b \simeq 0.11$, thus $\delta e/e \simeq 0.17$.

4 FITTING METHOD

For each of the 28 galaxies of the sample, a Levenberg–Marquardt algorithm was used to fit the minor axis surface brightness profile using the transformed major axis Sérsic law. The data for the major and minor axes light profiles are those analysed by CCD93.

The fit was performed for both the approximation of constant eccentricity, and for the more general case of variable eccentricity. We use the following notation:

$$\mu_{\rm c} = A_{\rm c} + \frac{B_{\rm c}}{e_{\rm c}} a^{1/n_a} \tag{20}$$

and

$$\mu_L = A_L + \frac{B_L}{e_0 n_a l} a^{1/n_a}\,\Phi\left(1 - \frac{\mathcal{F}(a)}{e_0}; 1; \frac{1}{n_a l}\right). \tag{21}$$

Equation (20) is for constant eccentricity and equation (21) is for variable eccentricity.

We decided to leave the parameters A and B completely free. The parameters n_a is the major axis Sérsic index measured by CCD93, while the parameters e_0 and l and the function $\mathcal{F}(a)$ are set by our fit to the eccentricity profiles. We noted that, ideally, the values we obtained for $A_{\rm c}$ and A_L should equal A_a while the values for $B_{\rm c}$ and B_L should be equal to B_a (where A_a and B_a are the values measured by CCD93.) Thus, the validity of our results, and hence of our proposed method, is determined by how close the above parameters are to their expected values.

The parameters obtained by fitting equations (20) and equation (21) to the CCD93 minor axis profiles are listed in Table 1, where for comparison we include the parameters found by CCD93.

In Appendix B we present the results of Table 1 in graphical format (Fig. B1); these figures also show the major axis profile. The bottom panel shows the residuals between the CCD93 data and our best-fitting model.

In Appendix A we present the fits to the eccentricity profiles (Fig. A1) derived from CCD93 data, the solid lines showing the

Table 1. Best-fitting Sérsic parameters (following the notation in equation 2): zero point A and scalelength B. A_a, A_b, B_a and B_b are the parameters measured by CCD93 on major (subscript a) and minor (subscript b) axes. A_c, A_L, B_c and B_L are the parameters computed by us for constant (subscript 'c') and variable (subscript 'L') eccentricity. The root mean square (rms) residuals of the fits are shown in the last three columns.

Galaxy	A_a	A_b	A_c	A_L	B_a	B_b	B_c	B_L	rms_b	rms_c	rms_L
NGC 4168	11.24	16.22	11.36	11.55	6.689	2.406	5.650	5.862	0.205	0.722	0.613
NGC 4261	8.17	13.05	8.61	9.11	8.852	4.760	6.900	7.085	0.692	0.892	0.666
NGC 4339	16.96	15.49	16.64	16.68	1.772	2.950	1.790	1.806	0.461	0.759	0.825
NGC 4360	17.10	15.21	16.88	17.15	2.190	3.850	1.894	1.950	0.459	0.827	1.156
NGC 4365	10.84	12.05	10.73	10.83	6.215	5.349	4.876	4.887	0.473	0.626	0.460
NGC 4374	7.60	9.48	7.60	5.23	8.682	7.299	8.373	8.338	0.339	0.315	0.458
NGC 4387	17.55	10.39	18.38	17.94	0.983	7.191	0.795	0.682	0.838	2.527	1.695
NGC 4406	0.44	8.08	−0.57	2.23	16.950	9.159	11.477	13.142	0.394	0.805	0.334
NGC 4415	19.55	17.69	19.68	19.72	0.640	1.921	0.576	0.568	1.407	0.669	0.754
NGC 4431	20.14	19.79	20.32	20.02	0.418	0.894	0.345	0.337	0.459	0.923	0.399
NGC 4434	14.00	16.46	13.83	14.00	4.053	2.111	4.011	3.945	0.996	0.639	0.455
NGC 4436	19.48	15.13	19.30	19.28	0.643	4.595	0.732	0.494	0.633	0.554	0.530
NGC 4458	17.28	18.17	16.86	16.64	1.635	1.168	1.614	1.661	3.313	1.399	1.130
NGC 4472	12.07	9.75	11.99	13.15	4.680	6.814	3.905	3.833	0.258	0.435	0.909
NGC 4473	15.73	5.27	15.53	14.52	1.897	11.238	1.360	1.287	0.330	1.872	0.957
NGC 4476	15.81	12.64	16.52	15.32	2.446	5.759	2.089	1.842	0.885	1.440	0.779
NGC 4478	16.99	16.25	17.07	16.92	0.954	1.474	0.904	0.883	0.883	0.481	0.397
NGC 4486	12.57	11.25	11.73	13.47	4.346	5.215	4.129	3.836	0.467	0.409	0.983
NGC 4550	18.07	17.30	17.41	17.75	0.468	1.149	0.321	0.359	0.758	0.584	0.923
NGC 4551	17.97	16.87	17.97	17.71	0.816	1.754	0.711	0.719	1.079	0.840	0.620
NGC 4552	−3.97	−0.61	−3.94	−1.52	20.087	16.850	17.816	17.982	1.205	1.241	1.040
NGC 4564	18.57	10.48	17.36	17.28	0.329	6.819	0.454	0.349	0.298	1.796	1.667
NGC 4600	20.10	18.16	19.89	19.83	0.163	1.484	0.206	0.175	0.550	0.567	0.442
NGC 4621	12.17	1.52	12.07	11.66	4.714	15.363	4.641	3.556	0.590	0.590	0.293
NGC 4623	19.98	16.89	19.68	20.15	0.130	2.302	0.130	0.096	0.104	2.588	3.749
NGC 4636	15.69	16.13	14.80	15.75	2.608	2.069	2.246	2.407	1.054	1.062	1.203
NGC 4649	12.70	10.34	12.58	12.31	4.038	6.122	3.499	3.416	0.797	0.725	0.595
NGC 4660	14.98	6.55	14.76	14.20	2.140	10.251	2.133	1.671	0.711	0.976	0.476

least-squares fit of the function given by equation (9) to the data points. For some galaxies, we could not use the parameters obtained by this fit and had to determine them interactively. In fact, the Lerch Φ critical radius a_c (Appendix C) must be larger than the largest observed radius, for the Lerch Φ function to converge in the radial interval covered by CCD93 observations. The eccentricity profile parameters are shown in Table 2.

5 THE RESULTS

The analysis of the results shown in Table 1 reveals an overall good agreement between the computed and the expected values.

For 14 of the galaxies, both A_c (the zero point in the constant eccentricity model) and A_L (the zero point in the variable eccentricity model) differ by less than 0.5 mag from the best-fitting A_a values determined by CCD93. For further eight galaxies the difference for both coefficients is less than 1 mag. The galaxies with the greatest discrepancies are NGC 4406, 4374 and 4552 for which $|A_L - Aa| > 1.5$ mag.

As for scalelengths (the B parameters in Table 1), 15 galaxies have B_c and B_L values which both differ by less than 20 per cent from B_a, while for eight galaxies the difference is less than 30 per cent, the object with the greatest discrepancy is NGC 4564 for which $|B_c - B_a|/B_a = 0.38$.

Fig. 3 shows how the minor axis Sérsic parameters, derived using our method, correlate well with the major axis parameters, this new correlation is a remarkable improvement over that shown in Fig. 2. The fact that the values of A_c, A_L, B_c, B_L are close to their expected values (A_a and B_a) indicates that our transformed major axis Sérsic models can fit the minor axis light profiles quite well.

These results support our proposal that the differences in the Sérsic model of the major and minor axes can be accounted for by radial variations of the isophotes eccentricity, indeed our model seems to be able to provide a valid mathematical description of the links between major and minor axes light profiles and the eccentricity profile.

There is increasing interest in using the $R^{1/n}$ law to address some issues related to the fundamental plane (FP) of elliptical galaxies (Ciotti, Lanzoni & Renzini 1996; Graham & Colless 1997; Ciotti & Lanzoni 1997), thus an extension of the work presented in our current paper would be to investigate how fitting the Sérsic model on different axes may affect the distribution of galaxies on the fundamental plane. This is because two galaxies with the same major axis light profile, but different eccentricity profiles, can give different values for the index n when the Sérsic model is fitted to their equivalent axis profile. This is because $R_{eq} = \sqrt{ab} = a\sqrt{e(a)}$, which may account for some of the scatter observed in the fundamental plane. A full study of this topic is, however, outside the scope of the present paper.

Table 2. Galaxy name, type and the eccentricity profile parameters. e_0 is the eccentricity at $a = 0$, e_1 the eccentricity at $a = a_M$, e_c is the value for the case of constant eccentricity, and l is the exponent.

Galaxy	Type	e_0	e_1	e_c	l	a_M
NGC 4168	E2	0.88	0.78	0.83	1.50	120
NGC 4261	E2	0.84	0.75	0.78	0.75	250
NGC 4339	S0(0)	0.95	0.86	0.93	2.00	120
NGC 4360	E2	0.90	0.75	0.81	0.80	120
NGC 4365	E3	0.75	0.66	0.74	3.50	300
NGC 4374	E1	0.70	0.96	0.93	0.15	380
NGC 4387	E5	0.60	0.76	0.80	1.22	110
NGC 4406	E3	0.88	0.57	0.65	0.35	700
NGC 4415	dE1, N	0.90	0.86	0.89	1.00	80
NGC 4431	dS0, N	0.53	0.75	0.65	1.35	72
NGC 4434	E0	0.96	0.82	0.95	2.50	84
NGC 4436	dS0, N	0.47	0.60	0.70	2.50	110
NGC 4458	E1	0.84	0.98	0.90	0.51	90
NGC 4472	E2	1.00	0.75	0.80	0.16	715
NGC 4473	E5	0.45	0.69	0.60	0.55	330
NGC 4476	S0(5)	0.58	0.91	0.85	0.75	154
NGC 4478	E2	0.82	0.97	0.88	3.00	77
NGC 4486	E0	1.00	0.60	0.85	0.65	550
NGC 4550	S0(7)	0.39	0.22	0.30	0.78	154
NGC 4551	E2	0.68	0.82	0.75	1.00	85
NGC 4552	S0(0)	1.00	0.81	0.88	0.43	300
NGC 4564	E6	0.44	0.61	0.60	1.00	190
NGC 4600	S0(6)	0.62	0.85	0.80	1.00	77
NGC 4621	E4	0.65	0.95	0.90	1.00	360
NGC 4623	E7	0.90	0.22	0.41	0.15	110
NGC 4636	E1	1.00	0.62	0.72	0.39	400
NGC 4649	S0(2)	0.77	0.83	0.82	0.60	640
NGC 4660	E3	0.55	0.86	0.82	0.70	130

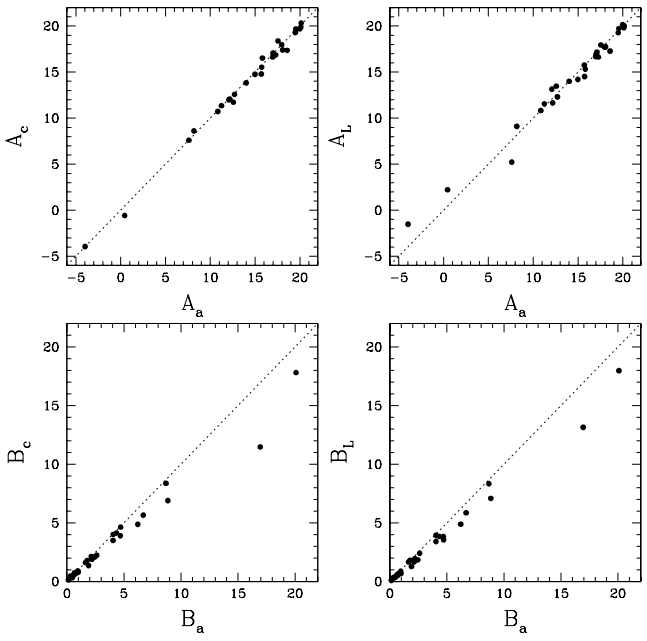

Figure 3. The relationship between the major axis parameters from CCD93 (A_a;B_a) and the parameters A_c, B_c, A_L and B_L derived in this paper. The scatter observed in Fig. 2 is here greatly reduced.

ACKNOWLEDGMENTS

This work was partially financed by CNPq.

REFERENCES

Binney J., Merrifield M., 1998, Galactic Astronomy. Princeton University Press, Princeton, NJ
Caon N., Capaccioli M., Rampazzo R., 1990, A&AS, 86, 429
Caon N., Capaccioli M., D'Onofrio M., 1993, MNRAS, 265, 1013 (CCD93)
Caon N., Capaccioli M., D'Onofrio M., 1994, A&AS, 106, 199
Ciotti L., 1991, A&A, 249, 99
Ciotti L., Lanzoni B., 1997, A&A, 321, 724
Ciotti L., Lanzoni B., Renzini A., 1996, MNRAS, 282, 1
de Vaucouleurs G., 1948, Ann. Astrophys., 11, 247
Gradshteyn I.S., Ryzhik I.M., 2000, Tables of Integrals, Series, and Products, 6th edn. Academic, San Diego, CA
Graham A., Colless M., 1997, MNRAS, 287, 221
Graham A., Trujillo I., Caon N., 2001a, AJ, 122, 1717
Graham A., Erwin P., Caon N., Trujillo I., 2001b, ApJ, 563, L11
Schombert J.M., 1986, ApJS, 60, 603
Sérsic J.L., 1968, Atlas de Galaxies Australes. Observatorio Astronomico, Cordoba, Argentina

APPENDIX A: ECCENTRICITY PROFILES

APPENDIX B: BRIGHTNESS PROFILES

In Fig. B1 we present the results of Table 1 in graphical format.

APPENDIX C: LERCH Φ FUNCTION

The Lerch Φ function (named after Mathias Lerch, 1860–1922) is defined as an infinite series (Gradshteyn & Ryzhik 2000)

$$\Phi(z, a, v) = \sum_{i=0}^{\infty} \frac{z^i}{(v+i)^a}, \tag{C1}$$

where $v + i \neq 0$. In the case studied in equation (13) we have

$$\Phi\left(1 - \frac{\mathcal{F}(a)}{e_0}; 1; \frac{1}{nl}\right) = \sum_{i=0}^{\infty} \frac{nl}{1+nli} \left[(1+l)\left(1 - \frac{e_1}{e_0}\right)\left(\frac{a}{a_M}\right)^l\right]^i. \tag{C2}$$

In this case ($a = 1$), one of the constraints for Φ to be finite is that we must have $|z| = |1 - \mathcal{F}(a)/e_0| < 1$, which corresponds to a critical radius a_c beyond which Φ is finite, given by

$$a_c \equiv \frac{a_M}{|(1+l)(1 - e_0/e_1)|^{1/l}}. \tag{C3}$$

We now may write equation (C2) in terms of a_c

$$\Phi\left(1 - \frac{\mathcal{F}(a)}{e_0}; 1; \frac{1}{nl}\right) = \sum_{i=0}^{\infty} \frac{nl}{1+nli} \left(\frac{a}{a_c}\right)^{l+i} \tag{C4}$$

The other constraint is that $1 + inl \neq 0$ in equation (C4) above, thus $nl \neq \ldots, -2, -1, 0$. When fitting the galaxy eccentricity profiles to equation (9) we must take these constraints into account.

The dependence of the Lerch Φ function on the n and l parameters is shown in Figs C1 and C2. Fig. C1 shows how Φ_L changes for values of $n = 1, 3, 5, 7, 9$, n raising in the direction indicated by the arrow. The solid curves have $l = 0.3$ and the dotted curves have $l = 0.7$. The same is true for Fig. C2, for which we plot the values $l = 1, \frac{1}{3}, \frac{1}{5}, \frac{1}{7}, \frac{1}{9}$, the solid curves having $n = 3$ and the dotted curves having $n = 9$. For all cases, $e_0 = 0.9$ and $e_1 = 0.1$. The critical radius a_c beyond which the function diverges should be noted. For example, in Fig. C1 the solid line has $a_c/a_M = 0.62$ and the dotted lines $a_c/a_M = 0.55$, cf. Equation (C4) and since a_c does not depend on n all the curves in Fig. C1 have the same critical radius.

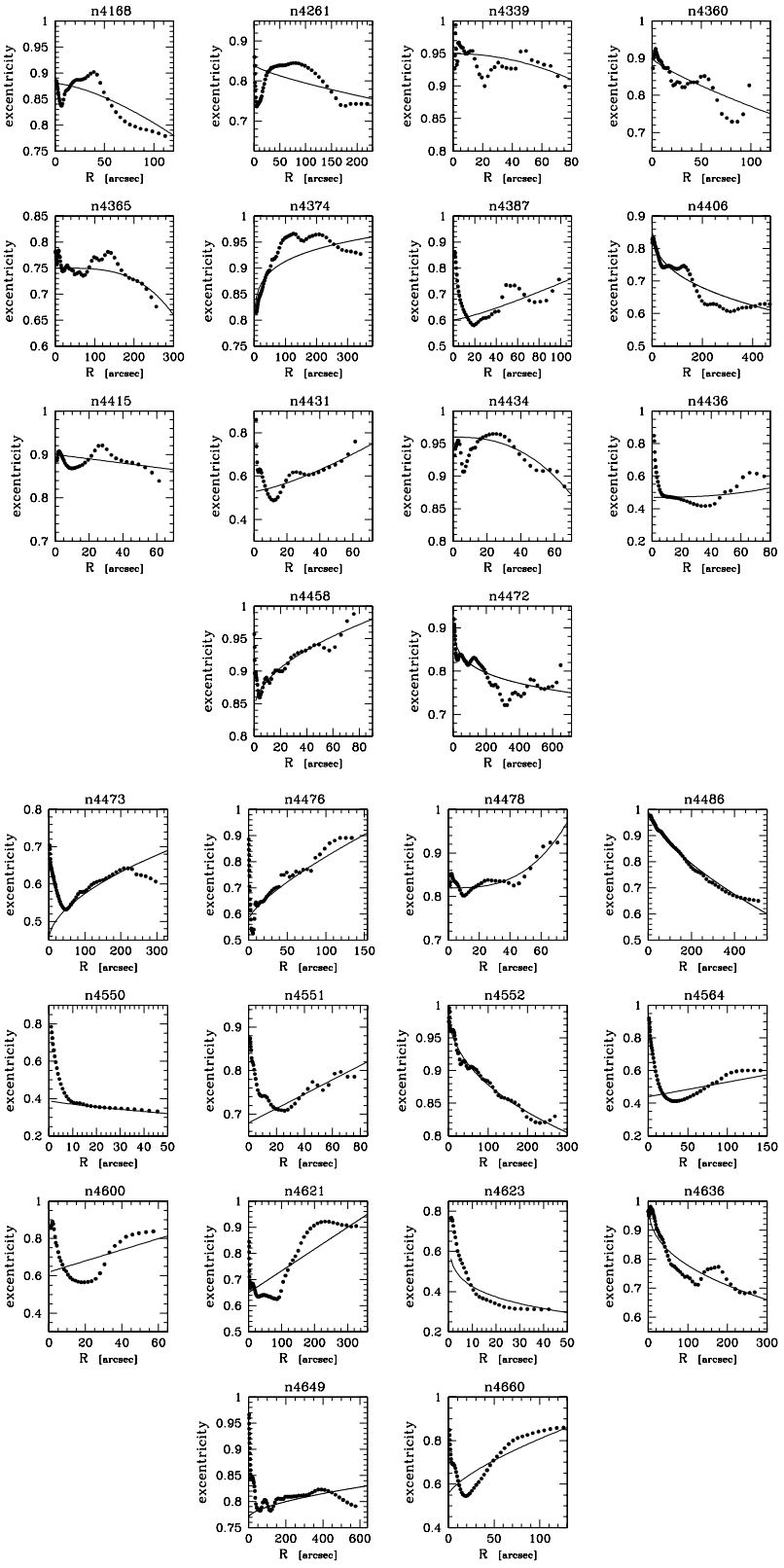

Figure A1. Eccentricity profiles. The dotted line shows the observed eccentricity from CCD93 data; the solid line is the least-squares fit of formula (9) to the data.

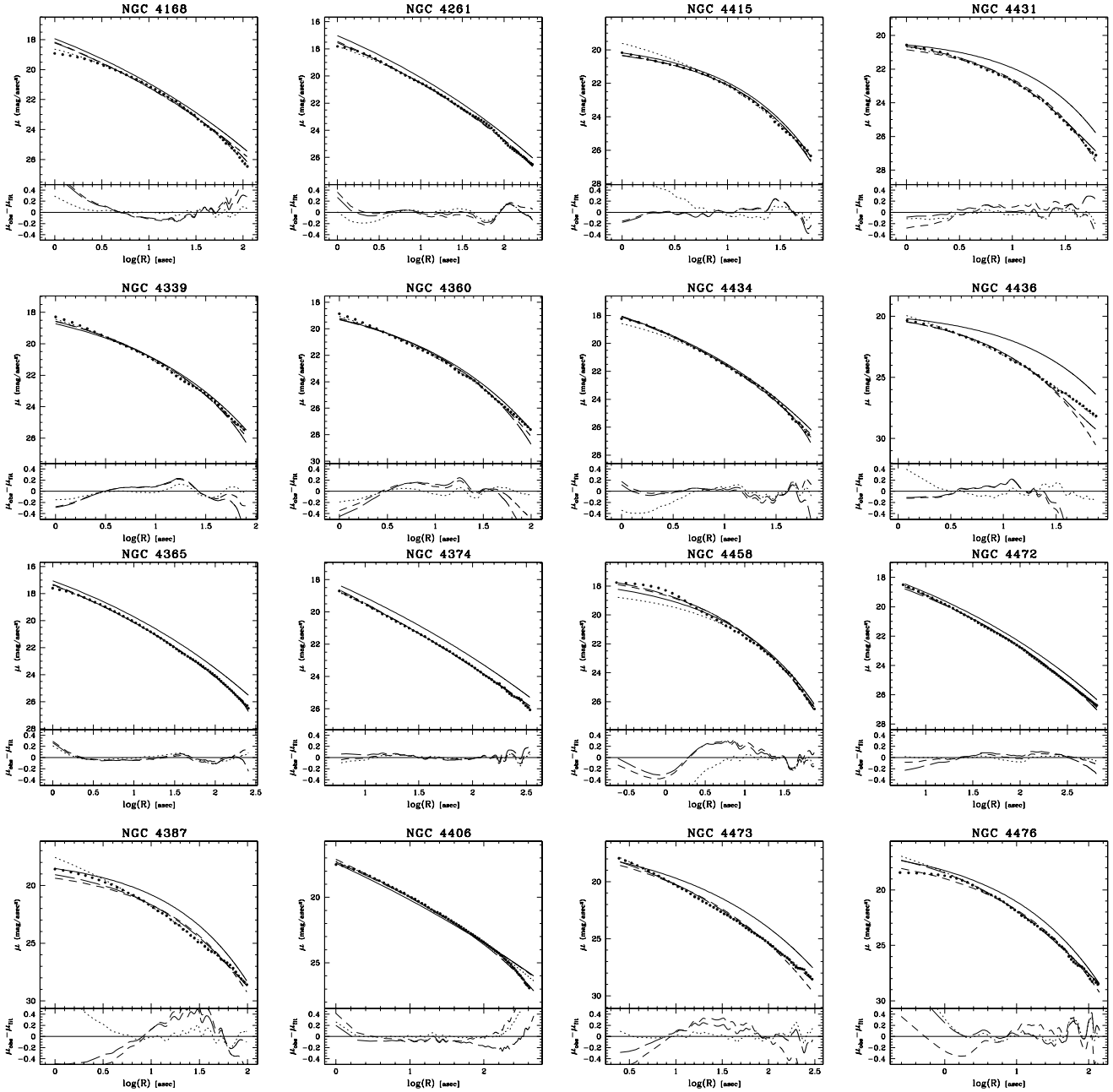

Figure B1. Surface brightness profiles. Solid and dotted lines represent the CCD93 Sèrsic fits to the galaxies major and minor axes profiles, respectively; the short and long dashed lines represent our transformation of the major axis Sèrsic law by constant and variable eccentricity, respectively. The bottom panel shows the residuals between the CCD93 data and the best-fitting models, using the same line styles as described above.

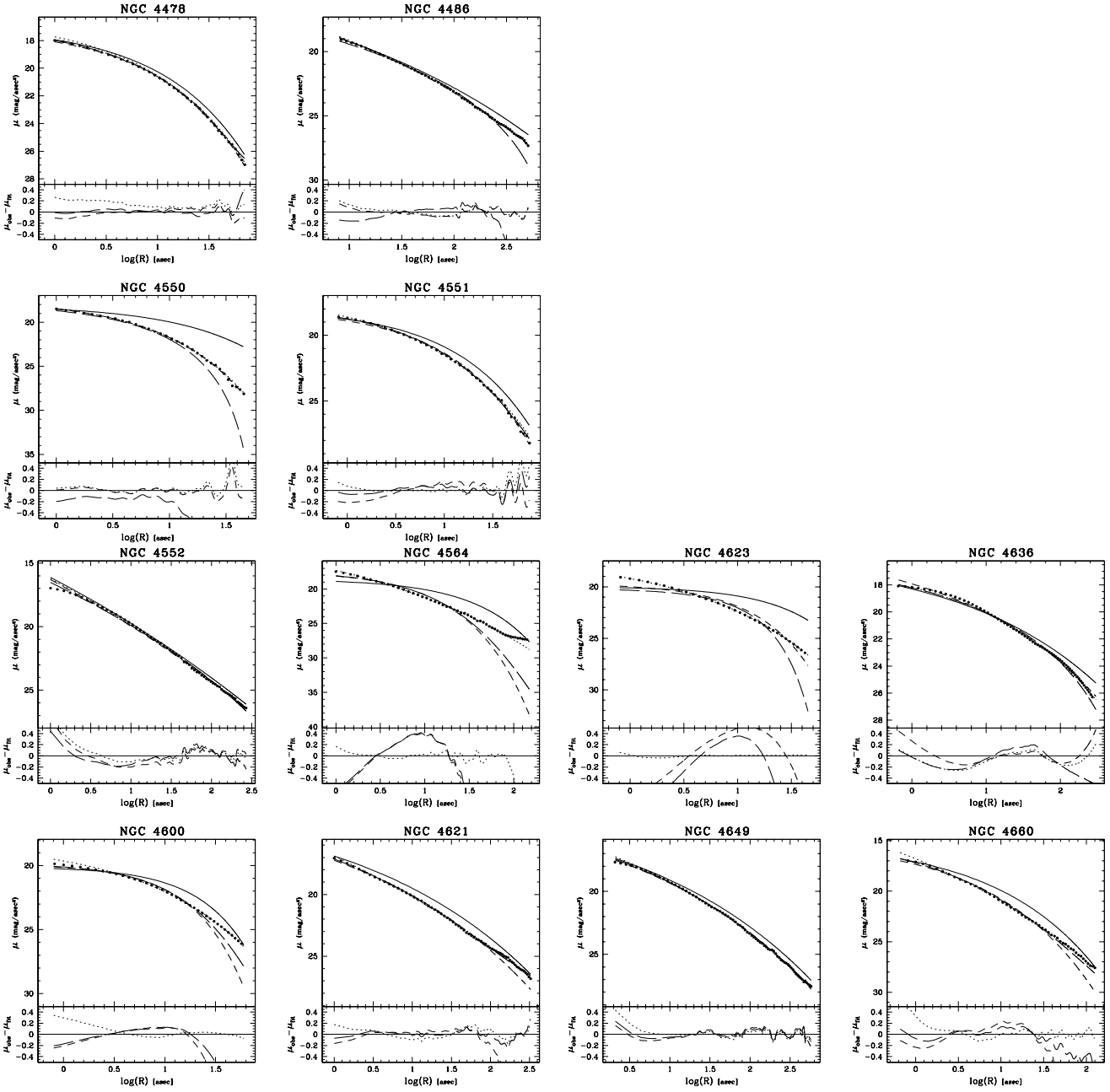

Figure B1 – Continued.

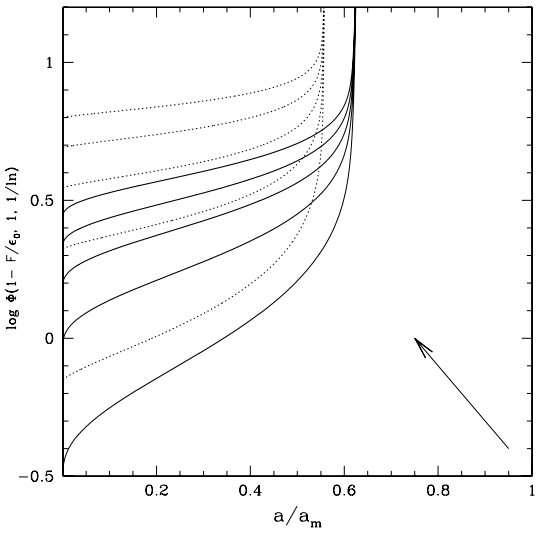

Figure C1. The dependence of the Lerch Φ function on the Sérsic index n. The plotted values are $n = 1, 3, 5, 7, 9$ increasing as indicated by the arrow. The solid lines are for $l = 0.3$ and the dotted lines for $l = 0.7$. In both cases $e_0 = 0.9$ and $e_1 = 0.1$.

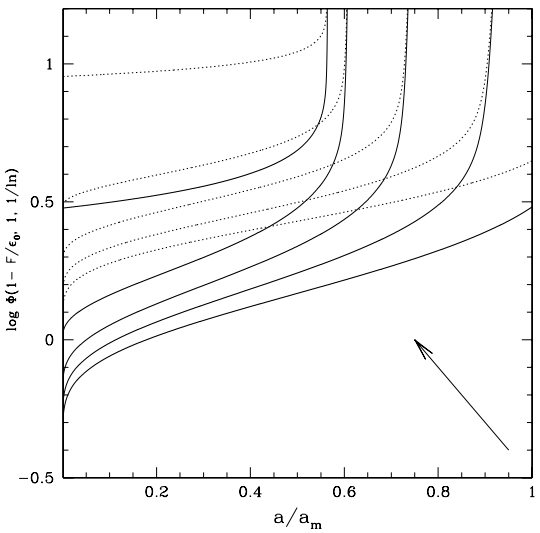

Figure C2. The dependence of the Lerch Φ function on the eccentricity parameter l. The plotted values are $l = 1, \frac{1}{3}, \frac{1}{5}, \frac{1}{7}, \frac{1}{9}$ increasing as indicated by the arrow. The solid lines are for $n = 3$ and the dotted lines for $n = 9$. In both cases $e_0 = 0.9$ and $e_1 = 0.1$.

This paper has been typeset from a TEX/LATEX file prepared by the author.